Cerâmica. 2025, v.71:eWSXD7406 http://dx.doi.org/10.1590/WSXD7406
ARTICLE

Optimizing flash sintering outcomes using response surface methodology

Fábulo Ribeiro Monteiro[1,*], João Vitor Campos[2], Gustavo César Dacanal[1,3], Lilian Menezes Jesus[4], Adilson Luiz Chinelatto[5], Eliria Maria de Jesus Agnolon Pallone[1,6], Rafael Vieira de Sousa[6]

[1] *University of São Paulo, USP/FZEA, Av. Duque de Caxias Norte, 225, 13635-900, Pirassununga, SP, Brazil*
[2] *Center for Research, Technology and Education in Vitreous Materials, Department of Materials Engineering, Federal University of São Carlos, UFSCAR, 13565-905 São Carlos, SP, Brazil*
[3] *Department of Food Engineering, University of São Paulo, USP/FZEA, Av. Duque de Caxias Norte, 225, 13635-900, Pirassununga, SP, Brazil*
[4] *Department of Physics, Federal University of de São Carlos, UFSCAR, Rod. Washington Luiz, w.o/n, 13565-905, São Carlos, SP, Brazil*
[5] *Department of Materials Engineering, State University of Ponta Grossa, UEPG, Av. General Carlos Cavalcanti, 474884030-900, Ponta Grossa, PR, Brazil*
[6] *Department of Biosystems Engineering, University of São Paulo, USP/FZEA, Av. Duque de Caxias Norte, 225, 13635-900, Pirassununga, SP, Brazil*

Abstract

Flash sintering, renowned for its rapid densification of ceramic materials, lacks comprehensive studies on the influence of electric field and current density on densification due to potential variations based on furnace type and sample geometry. This study introduces a computational modeling technique using response surface methodology to predict densification, onset temperature, and steady-state temperature in flash sintering. A mathematical model was developed to optimize densification in 8YSZ cylindrical and dog-bone samples, employing a central composite design combined with response surface methodology. Results predicted optimal electric field and current density values for densification across both geometries, elucidating their effects on onset and sample temperatures. Validation showed less than 5 % variation from experimental values, except for onset temperature and T_{BBR} in dog-bone samples, with 11 % and 13 % variations, respectively. These findings suggest the technique could be extended to incorporate additional process boundary conditions for different sample geometries, broadening its applicability.

Keywords: Response surface methodology; Central composite design; Optimization designs; Electric field assisted sintering; 8YSZ densification.

INTRODUCTION

Flash sintering (*FS*) is a promising technique due to the time it takes to happen (in the order of seconds) in furnace temperatures much lower than those used in other sintering techniques. It consists of applying an electric field (E) through the ceramic sample being heated in a furnace. At a certain critical temperature, the thermal runaway phenomenon occurs, quickly heating the sample and densifying it in a few seconds [1–5].

FS can be divided into three stages, characterized by their electric current values: stage (I) or incubation, during this initial stage, the applied voltage drives a relatively low electrical current through the sample. The resulting Joule heating is effectively dissipated into the environment, preventing any significant temperature rise; stage (II), or flash event, this is the defining stage of *FS*, marked by a sudden, nonlinear increase in electrical conductivity. As the current reaches a critical threshold, Joule heating surpasses the sample's ability to dissipate heat, triggering thermal runaway. This rapid temperature rise promotes enhanced mass transport, leading to accelerated densification; stage (III) or steady-state, in this final stage, the system stabilizes as the power supply switches to the current control mode. The sample temperature reaches a dynamic equilibrium, balancing heat generation and dissipation. Densification continues but at a slower rate compared to the flash event. The steady-state stage determines the final microstructure of the sample [3,6–9].

Also, according to studies conducted by Grasso et al. [10], it is estimated that *FS* heating rates reach values close to 10^4 °C.min^{-1}, depending on the parameters involved [10]. This heating rate favors densification with low grain growth, allowing the achievement of refined microstructures [11–14] with density values close to theoretical ones [15–17].

Despite the *FS* advantages, there are still some challenges to using this technique on an industrial scale, e.g., the need for conductive pastes to improve contact between sample and electrodes [18,19], difficulty in sintering homogeneously complex shape geometries [20,21], and the presence of thermal gradients among the specimens [15,22]. Furthermore, the importance of the ratio between surface

---

* fabulo.rm@usp.br
https://orcid.org/0000-0002-5176-6677

area and volume (*A/V*) in *FS* is emphasized as a limiting agent for the densification process. Some authors reported microstructural and densification heterogeneity, resulting from the thermal gradients generated in samples with volumes greater than their surface areas (e.g., the cylinders used in the present study, where the thickness and diameter result in a volume greater than the surface area) [23–25]. Currently, the literature lacks studies relating to the influence of *FS* parameters on different sample geometries.

In general, *FS* studies seek to design the ideal conditions for an adequate microstructure with a set of desired properties to enable the understanding of how these conditions relate to mass transport mechanisms, electrical conductivity, onset temperature, *FS* stage III temperature, and the final properties of sintered materials. However, reproducing the results from the literature involves many parameters since most of the furnaces and equipment used are adapted for *FS* and differ in terms of sample geometry, mode of application of electric current, and the applied *E* [26–28].

The experimental design and response surface methodologies (*RSM*) exhibit excellent applicability in the development of methods based on multiple variables [29,30]. Therefore, these methodologies can be applied to understand how variables affect flash sintered samples and enable finding the optimal conditions of the *FS* parameters (using a limited number of experiments), such as *E* and electric current density (*J*), among others, regardless of sample format.

One should also notice that *RSM* allows us to identify the appropriate parameters to be used in the process while minimizing the number of samples and time, making it advantageous for *FS*-related studies. Moreover, the technique allows us to optimize experimental responses by simultaneously assessing the variables involved in the process and identifying how they influence each other, and how they influence the final material properties and interactions [29,31,32].

In view of this, this study aimed to use the *RSM* technique to determine the ideal *E* and *J* values to optimize the densification of flash sintered 8YSZ cylindrical and dog-bone samples. Through interpolation and validation of mathematical models obtained via the *RSM* technique, the influence of *E* and *J* magnitudes on the densification, onset, and steady-state temperatures of flash-sintered samples was evaluated.

MATERIAL AND METHODS

The procedures for developing and validating the technique involve conducting experiments under different conditions to create a dataset for use in modeling and subsequently in the validation and exemplification of the model.

Commercial zirconia powder stabilized with 8 mol% yttria (*8YSZ*; TZ-8Y, Tosoh Corp., Japan) was used in sample preparation. For this, a suspension was prepared in an aqueous medium with 3.5 wt.% of the DURAMAX D-3005 dispersant and 2.5 wt.% of the DURAMAX B-1022 (Dow Chemical, USA) binder in a ball mill for 24 h. Then, the suspension was dried by hot air flow and passed through a 100-mesh sieve.

The resulting powder was compacted by uniaxial pressing, using 200-MPa pressure, in two geometries: cylindrical and dog-bone, as illustrated in Figure 1. After conformation, samples were calcined at 800 °C for 120 min, with a heating rate of 2 $°C.min^{-1}$ to remove the binder and the dispersant.

Figure 2 illustrates the tubular furnace used in *FS* [25], and how platinum electrodes were positioned in both sample geometries. Flash conditions were controlled by a programmable power supply (751iX II series, California Instruments) and data acquisition was done via the LabVIEW 2013 (NI) software.

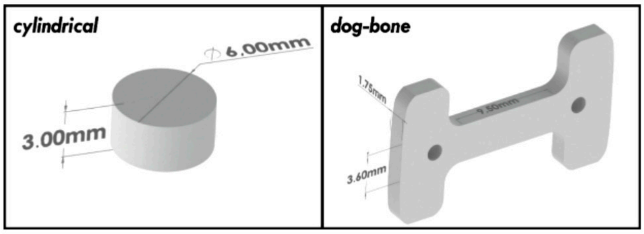

Figure 1: Dimensions of the “green samples” in cylindrical and dog-bone shapes.

For the experimental design, the atmosphere (ambient air), furnace heating rate (20 $°C.min^{-1}$), frequency of the applied *E* (1000 Hz), and flash time (60s) were fixed. The surface area to volume ratio (*A/V*) (through which the electric current passes) for the cylindrical and dog-bone samples was 1.33 and 1.91 mm^{-1}, respectively.

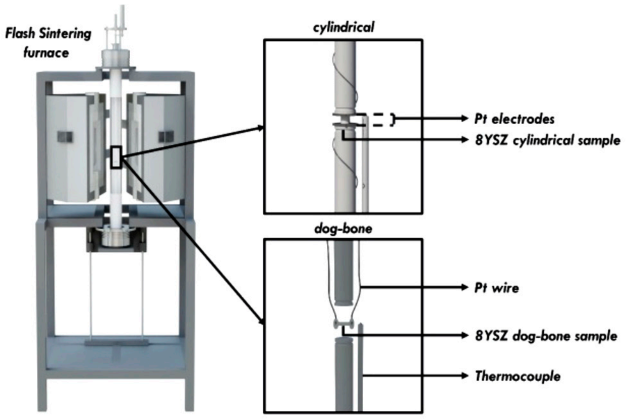

Figure 2: Representation of the furnace used for flash sintering, focusing on the positioning of the cylindrical and dog-bone samples.

Minimum and maximum values of *E* and *J* were, respectively, 80 and 200 $V.cm^{-1}$ and 80 and 200 $mA.mm^{-2}$, for both geometries. These were determined according to previous studies [33–36] and power supply limitations to assess a range of these variables that could be applied to our samples.

A central composite design (CCD) with three central points, combined with the *RSM*, was used to investigate the influence of *E* and *J* on densification, onset temperature, and the black body radiation (*BBR*) model-estimated temperature during the *FS* steady-state of 8YSZ samples, resulting in 11 experiments.

With the boundary values of the independent variables defined (representing the manipulated *E* and *J* values in the experiment), the Statistica software (v. 13.5, StatSoft, Tulsa, USA) was used to derive the experimental conditions under examination. The operational conditions used in experimental design, represented by variables *E* (V.cm^{-1}) and *J* (mA.mm^{-2}), and their coded values X_1 and X_2 are shown in Table 1. Coded variables were used since they allow us to observe the relative importance of the effects. The comparative analysis of the selected geometries was based on the response surfaces obtained by the variables encoded at levels -1.41, -1.00, 0.00, 1.00, and 1.41. Applying coded variables (as 1.00 and -1.00) is common to dimensionalize experimental levels and is called coding the data. This coding aids in the interpretation of the coefficients fit to any experimental model. After factor settings are coded, center points have the value "0.00". It is a simple linear transformation of the original measurement scale.

With *E* and *J* combinations generated by experimental design (Table 1), 8YSZ cylindrical and dog-bone samples were subjected to *FS*. Then, the relative density (*ρ*) was measured using Archimedes' principle, according to ASTM C373-18 [37]. The mean values of relative densities were expressed according to theoretical density.

Table 1 - Values for *E* (V.cm^{-1}) and *J* (mA.mm^{-2}) and their respective coded variables, X_1 and X_2, applied to experimental design.

Run	*E* (X_1)	*J* (X_2)
1	97.60 (-1.00)	97.60 (-1.00)
2	97.60 (-1.00)	182.00 (1.00)
3	182.00 (1.00)	97.60 (-1.00)
4	182.00 (1.00)	182.00 (1.00)
5	80.00 (-1.41)	140.00 (0.00)
6	200.00 (1.41)	140.00 (0.00)
7	140.00 (0.00)	80.00 (-1.41)
8	140.00 (0.00)	200.00 (1.41)
9	140.00 (0.00)	140.00 (0.00)
10	140.00 (0.00)	140.00 (0.00)
11	140.00 (0.00)	140.00 (0.00)

FS onset temperature was measured immediately before the power supply changed from voltage to electrical current control. The estimated temperature of the samples in the steady-state (stage III) was estimated by the *BBR* model [38], as shown in Eq. (A):

$$T_S = T_0^4 + \left(\frac{W}{A= \epsilon\sigma_S}\right)^{1/4} \qquad \text{(A)}$$

where T_S is the estimated sample temperature; T_S, the furnace temperature; *A*, the total surface area of the sample (assumed as the measurement section); ϵ refers to the material emissivity (ϵ=0.9 is the emissivity of most oxides); W is the electrical power dissipation; and σ_S , the Stefan-Boltzmann constant, equivalent to 5.67 × 10^{-8} W.m^2. K^{-4}.

To estimate sample temperature (T_{BBR}) in the steady-state, the data obtained in the last 5 s of sintering were used, thus ensuring that *E* and *J* values were already stabilized.

Both geometries subjected to *FS* and the values of each dependent variable were used to estimate the coefficients of a polynomial model, as shown in Eq. (B):

$$Y=\beta_0+\beta_1X_1+\beta_2X_{2+}\,\beta_{11}X_1^2+\beta_{22}X_2^2+\beta_{12}X_1X_2 \qquad \text{(B)}$$

where Y is the estimated response, X_i, the independent coded variable of the process at scale, and β_i , the model coefficient for the variable i. Variance analysis (ANOVA), the lack-of-fit test, regression coefficient determination, and response surface generation were performed in the Statistica software. Only statistically significant coefficients ($p < 0.05$) were maintained in the regression and generation of response surface models.

In the second modeling stage, the most desirable points for the process were obtained. The equations obtained by the Design of Experiments (*DoE*) method were delimited by a set of contour constraints determined by the generated response surfaces and the qualitative analyses of the sintered samples.

As an example, the most desirable process points were obtained within defined boundaries. Optimization was performed from a set of constraints determined according to the results for response surfaces. To prevent temperatures that may induce sample melting, onset values ranging from 700 to 900 °C were selected, and a maximum T_{BBR} of 2000 °C. Table 2 shows the constraint sets used to determine the optimized parameters for best densification according to these boundaries.

Mathematica software optimization tool (see 12.3.1, Wolfram Research, Inc., USA) was used to determine the most desirable *E* and *J* operating conditions, i.e., those in which high densification occurs. The experimental validation of the optimal points allowed the comparison between the cylindrical and dog-bone geometries.

RESULTS AND DISCUSSION

Computational modeling was carried out on three fronts to acquire the three types of predictive models: one for densification, another for onset temperature, and a third for

Table 2 - Constraint values used to optimize the densification of sintered samples.

Parameter	Restriction
E (V.cm^{-1})	$80 \leq E \leq 200$
J (mA.mm^{-2})	$80 \leq J \leq 200$
Onset (°C)	700 ≤ *Onset* ≤ 900
T_{BBR} **(°C)**	≤2000

steady-state temperature. The outcomes from each modeling process and validation are delineated in the subsequent sections.

Table 3 summarizes the results obtained via experimental design for 8YSZ samples in both geometries. In the *E* and *J* columns, it is possible to find the (operational and coded) independent variables generated by experimental design. The remaining columns show the other results obtained by sintering with the *E* and *J* combinations generated by experimental design (dependent variables).

For the central points 140.00 (0.00), dispersions in the values of ρ, Onset, and T_{BBR} were observed as 0.6%, 14.5°C, and 7.4°C for cylindrical samples, and 2.1%, 29°C, and 96°C for dog-bone samples, respectively.

Based on the results obtained through experimental design, regression coefficients for coded second-order polynomial equations were determined (β_i) (Eq. B), the ratio values between variances (F), probability (p), and determination coefficients (R^2), as shown in Table 4.

The resulting equations were tested through variance analysis (ANOVA). The adjusted models demonstrated adequacy, exhibiting significant regression, low residual values, lack-of-fit, and satisfactory determination coefficients. Figs. S1, S2, and S3 (supplementary material) present the residual plots of the predicted versus observed values, comparing the models considering the non-significant values with the models in which the non-significant values were discarded. As expected, the model is not significantly altered when the non-significant values are considered. Furthermore, the linear relationships between predicted and observed values indicate a strong correlation between the results obtained with the experimental data and those generated with the model.

Figure 3 shows the response surfaces for the relative density of cylindrical and dog-bone-shaped samples. Both surfaces indicate that the *E* values have a negligible impact on densification. As Table 4 shows, the β_1 and β_{11} coefficients, referring to linear and quadratic *E* values, respectively, were non-significant in the relative density equation used for both geometries. These results corroborate the findings from the literature [19,33,36,39], in which densification directly relates to the applied *J* magnitude, rather than to the *E* value.

Table 3 - Independent (operational and coded) and dependent variables (results) used in our experimental design to obtain regression coefficients.

	Run	E (V.cm^{-1}) (X_1)[a]	J (mA.mm^{-2}) (X_2)[a]	ϱ (%DT)[b]	Onset (°C)[b]	T_{BBR} (°C)[b]
Cylindrical	1	97.60 (-1.00)	97.60 (-1.00)	81	804	1504
	2	97.60 (-1.00)	182.00 (1.00)	91	801	1885
	3	182.00 (1.00)	97.60 (-1.00)	82	715	1579
	4	182.00 (1.00)	182.00 (1.00)	92	718	1977
	5	80.00 (-1.41)	140.00 (0.00)	84	825	1681
	6	200.00 (1.41)	140.00 (0.00)	90	704	1765
	7	140.00 (0.00)	80.00 (-1.41)	80	747	1490
	8	140.00 (0.00)	200.00 (1.41)	87	753	1999
	9	140.00 (0.00)	140.00 (0.00)	87	751	1760
	10	140.00 (0.00)	140.00 (0.00)	88	727	1763
	11	140.00 (0.00)	140.00 (0.00)	88	753	1749
Dog-bone	1	97.60 (-1.00)	97.60 (-1.00)	93	817	1275
	2	97.60 (-1.00)	182.00 (1.00)	97	801	1555
	3	182.00 (1.00)	97.60 (-1.00)	94	748	1446
	4	182.00 (1.00)	182.00 (1.00)	95	716	1658
	5	80.00 (-1.41)	140.00 (0.00)	98	904	1451
	6	200.00 (1.41)	140.00 (0.00)	96	728	1510
	7	140.00 (0.00)	80.00 (-1.41)	92	759	1257
	8	140.00 (0.00)	200.00 (1.41)	98	721	1665
	9	140.00 (0.00)	140.00 (0.00)	98	728	1497
	10	140.00 (0.00)	140.00 (0.00)	95	708	1601
	11	140.00 (0.00)	140.00 (0.00)	94	765	1410

Independent variable values (those between brackets are coded variables).[B] Experimental design results. ρ: apparent density (%DT); Onset: flash starting temperature (°C); and T_{BBR}: estimated temperature of black body radiation at the stationary stage (°C), respectively.

Table 4 - Coded second-order regression coefficients for apparent density, onset, and *BBR* temperature for cylindrical and dog-bone samples.

	Coef.	ρ (%DT)	*Onset* (°C)	T_{BBR} (°C)
Cylindrical	β_0	84.43	747.27	1751.89
	β_1	NS	-42.75	35.65
	β_2	3.77	NS	187.22
	β_{11}	NS	9.85	-14.88
	β_{22}	NS	NS	NS
	β_{12}	NS	NS	NS
	R^2	0.66	0.96	1.00
	F	17.46	219.19	1717.68
	p-value	<0.002	<0.017	<0.023
Dog-bone	β_0	95.27	732.75	1484.00
	β_1	NS	-50.12	NS
	β_2	1.78	NS	133.7
	β_{11}	NS	38.96	NS
	β_{22}	NS	NS	NS
	β_{12}	NS	NS	NS
	R^2	0.50	0.87	0.77
	F	8.98	37.51	29.9
	p-value	<0.015	<0.000	<0.000

NS: Non-significant (p > 0.05).

Variations in relative density values and the *J* value (β_2 coefficients in Table 3) are more significant for cylindrical samples than for dog-bone samples, possibly due to the surface area-to-volume ratio (*A/V*) values. The applied *J* is equal for both sample types and is directly related to the densification and temperature of the process. However, our cylindrical samples have a larger cross-sectional area and a greater surface area in contact with the metallic electrodes. In this case, this difference is associated with the joule heat dissipated during the process and transferred to the environment (via conduction to the electrodes, convection, and radiation to the furnace air).

Studies by Grimley et al. [20] and Campos et al. [40] showed that the surface area to volume ratio (*A/V*) limits *FS*. Depending on the free surface area, thermal and microstructural heterogeneity are observed in the sample [20,40]. This is directly related to material densification. Possibly due to this, dog-bone samples showed higher relative density values than cylindrical ones, when using the same electrical parameters. Thus, the geometry effects (*A/V*) and the presence of the metallic electrode in cylindrical samples result in greater heat loss compared to dog-bone samples, leading to reduced densification.

Figure 4 shows the onset temperature behavior as a function of *E* and *J* for cylindrical and dog-bone format samples, respectively. According to the results, onset temperature is strongly affected by the applied *E*, dramatically falling as *E* increases. *J* variation failed to show a significant influence on onset temperature. These findings also corroborate the results observed in the literature [7,36,41].

The response surfaces for onset temperature show a slightly concave curvature due to the β_{11} coefficient, which was significant for these surfaces. Furthermore, dog-bone surfaces show a greater sensitivity to increasing *E* values, as the larger green region in Figure 4 and the β_1 and β_{11} values show. This difference is possibly due to thermal losses by conduction to the electrodes occurring in cylindrical samples since electrical contact is made with the use of platinum discs on flat surfaces for this geometry. In this configuration, a significant amount of heat is dissipated by conduction to the electrodes. So, for the same *E* and *J* conditions, cylindrical samples will require a higher furnace temperature to achieve onset than dog-bone ones [22,27,40].

Figure 5 shows the response surfaces for the temperature estimated by the *BBR* mathematical model during the *FS* steady-state. When analyzing the regression coefficients for T_{BBR} (Table 4), a notable influence of the β_2 coefficient on *J* was observed in both samples. Moreover, the β_{11} coefficient

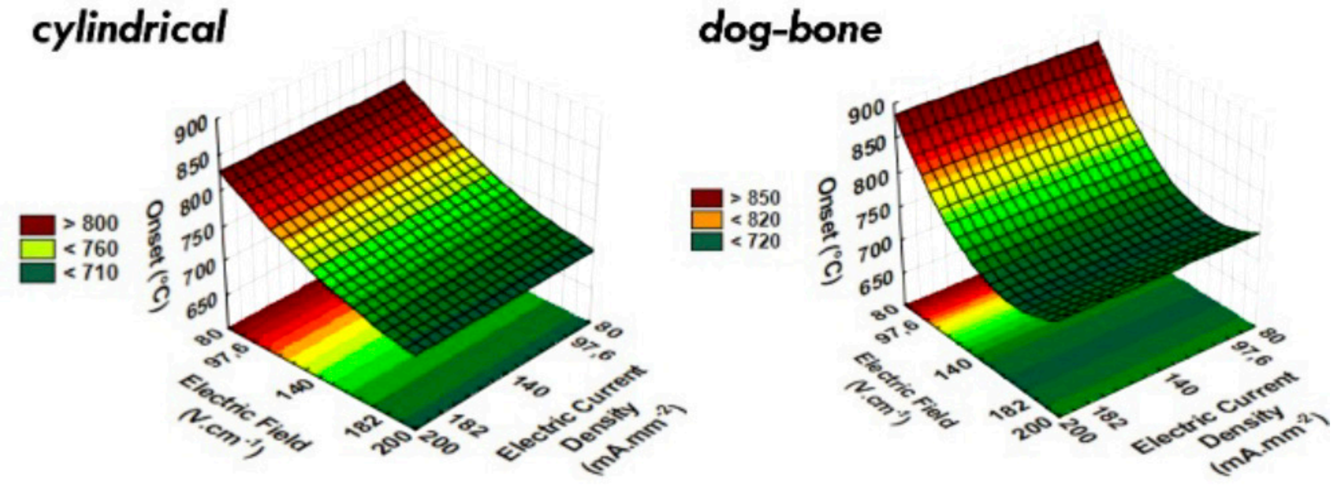

Figure 3: Response surface of relative density (%DT) of cylindrical and dog-bone samples.

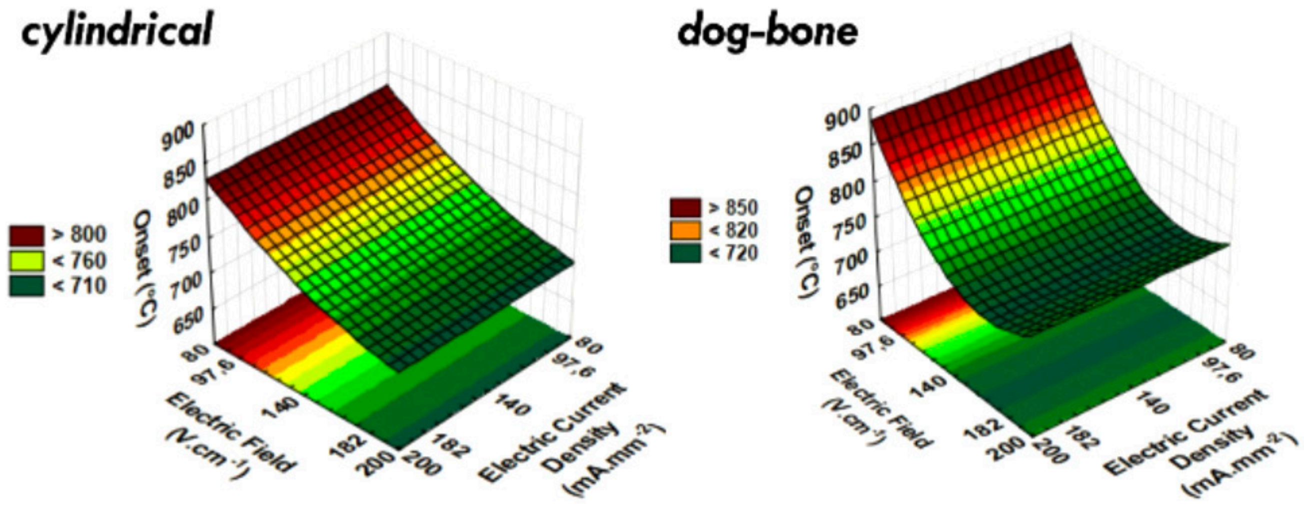

Figure 4: Response surface for the onset temperature of the flash event in cylindrical and dog-bone samples.

negatively contributed to the response surface of cylindrical samples, explaining their convex curvature (Figure 5).

Higher temperatures and a broader temperature range were observed in cylindrical samples compared to those in dog-bone samples. By comparing T_{BBR} (Figure 5) and relative density surfaces (Figure 3). This can explain the more pronounced variation in the relative density values observed in cylindrical samples (Figure 3). The estimated temperatures for dog-bone samples under different conditions showed very close values, explaining their smaller density variation. Furthermore, as shown, cylindrical samples tend to reach higher T_{BBR} values than those estimated for dog-bone samples. Thus, during sintering, a higher power is provided for densification. However, the density values were, in general, lower for cylindrical samples, likely due to the microstructural heterogeneity usually observed for this geometry [40].

The T_{BBR} difference is related to thermal losses. As discussed earlier, heat dissipation by conduction to the platinum electrodes during cylindrical sample sintering causes lower electrical conductivity. Thus, the flash event happens at a higher furnace temperature for cylindrical samples than dog-bone ones. Since T_{BBR} estimates raise furnace temperatures to the fourth power, as Eq. **(A)** shows, this explains the increase in the estimated temperature for cylindrical samples.

Utilizing the constraints specified in Table 2, optimized values for E and J were estimated. Subsequently, *FS* was conducted using the obtained values to validate the optimized mathematical model. Cross-validation was also executed to assess the models' generalization capacity, with the objective of evaluating their accuracy and subjecting them to testing with all available data.

Table 5 shows the predicted and experimental ρ, onset, and T_{BBR} values obtained for the validation *FS* and the cross-validation of the mathematical models using the optimized *E* and *J* values obtained by the Mathematica software.

As can be seen, the predicted and experimental values agree well. Validation and cross-validation results exhibit

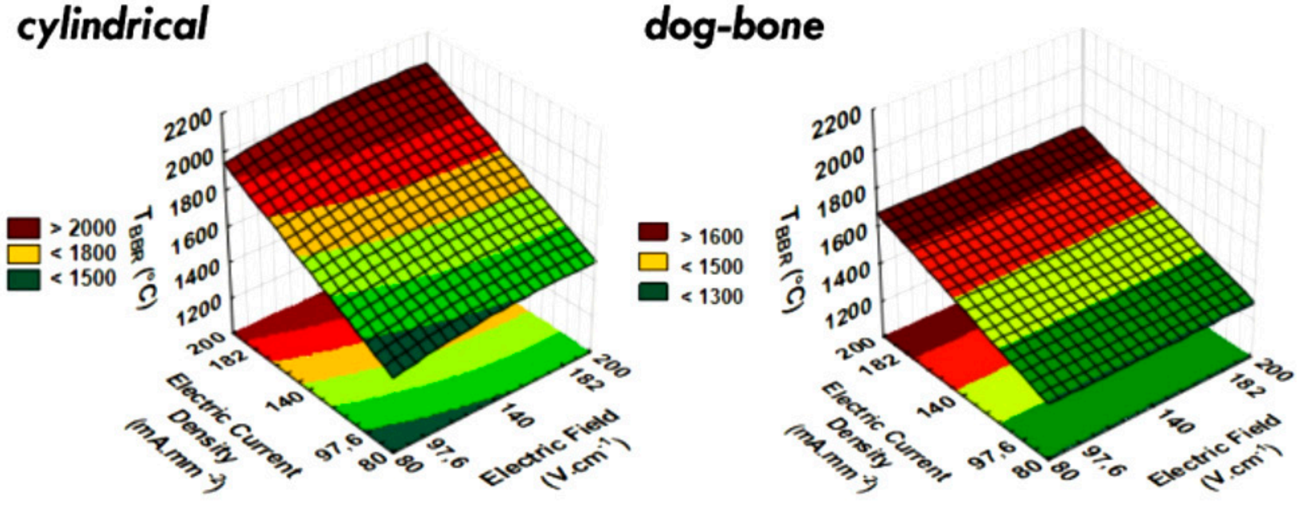

Figure 5: Response surface for the temperature estimated by *BBR* in cylindrical and dog-bone samples.

Table 5 Values of ρ, *onset,* and T_{BBR} obtained using the values of E and J, optimized by the Mathematica software, for validation and cross-validation of the mathematical models obtained.

Run	Sample[a]	E (V.cm^{-1})[b]	J (mA.mm^{-2})[b]	Result[a]	ρ (%DT)	Onset (°C)	T_{BBR} (°C)
Validation	CL	122.75	200.00	Pred.	90	766	2000
				Expe.	87	765	2024
	DB	197.00	200.00	Pred.	98	736	1673
				Expe.	96	652	1888
Cross-validation	CL	197.00	200.00	Pred.	90	708	2000
				Expe.	87	722	2074
	DB	122.75	200.00	Pred.	98	737	1670
				Expe.	97	776	1728

[a] *Abbreviations used to represent the samples: CL - Cylindrical and DB - Dog-bone, and to describe the results:* ***Pred.*** *- Predicted by the mathematical model and Expe. - Obtained by the experimental performance.*
[b] *Electric field (E) and electric current density (J) values obtained by optimization and used in sintering.*

a variation of less than 5 % between the values estimated by the optimized models and the experimental values, except for onset temperature and T_{BBR} in the validation of dog-bone samples, which showed an 11 % and 13 % variation, respectively. When performing the cross-validation, the density value obtained for dog-bone samples was slightly higher than that obtained by optimization validation. Furthermore, experimental T_{BBR} values for the cylindrical samples were higher than the restriction value for the optimization model (2000 °C). These variations may relate to physical and microstructural characteristics that were ignored in the used models, such as grain size, real sample emissivity, activation energy, and electrical conductivity, among others. Irrespective of that, in general, we found no significant differences between the estimated and experimental values, indicating that the methodologies applied here are efficient for designing *FS* experiments.

CONCLUSIONS

The utilization of the RSM technique demonstrated effectiveness in acquiring optimal E and J values to enhance the densification process of flash-sintered 8YSZ cylindrical and dog-bone samples. Furthermore, it facilitated comprehension and prediction of the influence of E and J values on ρ, onset temperature, and T_{BBR}. One of the key benefits of this statistical approach is its ability to predict the best processing conditions with a limited number of experiments, making it highly efficient for materials with high costs or limited quantities. This capability is especially valuable when considering the scaling-up of the technique. Thus, *RSM* optimization emerges as an efficient tool for determining optimized *FS* parameters across samples with varied geometries, enabling correlation among multiple variables inherent to the process and understanding their trends and interrelations. Future studies could extend this statistical methodology to encompass boundary conditions applied to different sample geometries.

ACKNOWLEDGMENTS

This work was supported by the Coordenação de Aperfeiçoamento de Pessoal de Nível Superior – Brasil (CAPES) – Finance Code 001 and the São Paulo Research Foundation (FAPESP) [2015/07319-8, 2018/19370-6, 2019/14677-9, 2021/06509-9 and 2023/18168-7].

REFERENCES

[1] Dong J, Wang Z, Zhao X, Biesuz M, Saunders T, Zhang Z, et al. Contactless flash sintering based on cold plasma. *Scr Mater*. 2020;**175**:20-23. doi:10.1016/j.scriptamat.2019.08.039.
[2] Wang X, Zhu Y, Huang R, Mei H, Jia Z. Flash sintering of ZnO ceramics at 50 °C under an AC field. *Ceram Int*. 2019;**45**:24909-13. doi:10.1016/j.ceramint.2019.08.142.
[3] Yang B, Phuah XL, Shang Z, Sheng X, Wang H, Zhang X. Effects of incubation on microstructure gradient in flash-sintered TiO2. *Scr Mater*. 2022;**207**:114270. doi:10.1016/j.scriptamat.2021.114270.
[4] Ojaimi CL, Ferreira JA, Chinelatto AL, Chinelatto ASA, Pallone EMJA. Microstructural analysis of ZrO2/Al2O3 composite: Flash and conventional sintering. *Ceram Int*. 2020;**46**:2473-80. doi:10.1016/j.ceramint.2019.09.241.
[5] Campos JV, Lavagnini IR, Avila V, Yoon B, Ghose S, Raj R, et al. On the Arrhenius-like behavior of conductivity during flash sintering of 3 mol% yttria stabilized zirconia ceramics. *Scr Mater*. 2021;**203**:114093. doi:10.1016/j.scriptamat.2021.114093.
[6] Lu S, Liu J, Shao G, Liu W, Zhao R, Liu D, et al. On the electric conduction of ZrO2 in the steady stage of flash sintering. *Ceram Int*. 2020;**46**:5715-18. doi:10.1016/j.ceramint.2019.11.019.
[7] Jo S, Raj R. Transition to electronic conduction at the onset of flash in cubic zirconia. *Scr Mater*. 2020;**174**:29-32. doi:10.1016/j.scriptamat.2019.07.043.
[8] Wang H, Phuah XL, Charalambous H, Jha SK, Li J, Tsakalakos T, et al. Staged microstructural study of flash

sintered titania. *Materialia*. 2019;**8**:100451. doi:10.1016/j.mtla.2019.100451.

[9] Jha SK, Raj R. Electric fields obviate constrained sintering. *J Am Ceram Soc*. 2014;**97**:3103-9. doi:10.1111/jace.13136.

[10] Grasso S, Sakka Y, Rendtorff N, Hu C, Maizza G, Borodianska H, Vasylkiv O. Modeling of the temperature distribution of flash sintered zirconia. *J Ceram Soc Japan*. 2011;**119**:144-46. doi:10.2109/jcersj2.119.144.

[11] Liu D, Liu J, Gao Y, Liu F, Li K, Xia J, et al. Effect of the applied electric field on the microstructure and electrical properties of flash-sintered 3YSZ ceramics. *Ceram Int*. 2016;**42**:19066-70. doi:10.1016/j.ceramint.2016.09.065.

[12] Lavagnini IR, Campos JV, Pallone EMJA. Microstructure evaluation of 3YSZ sintered by Two-Step Flash Sintering. *Ceram Int*. 2021;**47**:21618-24. doi:10.1016/j.ceramint.2021.04.174.

[13] Carvalho S, Muccillo E, Muccillo R. Electrical behavior and microstructural features of electric field-assisted and conventionally sintered 3 mol% yttria-stabilized zirconia. *Ceramics*. 2018;**1**:3-12. doi:10.3390/ceramics1010002.

[14] Valdebenito JU, Akbari-Fakhrabadi A, Viswanathan MR. Effect of flash sintering on microstructure of Ce0.9Gd0.1O1.95 electrolyte fabricated by tape-casting. *Mater Lett*. 2017;**209**:291-94. doi:10.1016/j.matlet.2017.07.129.

[15] Grimley CA, Funni S, Green C, Dickey EC. A thermal perspective of flash sintering: The effect of AC current ramp rate on microstructure evolution. *J Eur Ceram Soc*. 2021;**41**:2807-17. doi:10.1016/j.jeurceramsoc.2020.11.040.

[16] Steil MC, Marinha D, Aman Y, Gomes JRC, Kleitz M. From conventional AC flash-sintering of YSZ to hyper-flash and double flash. *J Eur Ceram Soc*. 2013;**33**:2093-101. doi:10.1016/j.jeurceramsoc.2013.03.019.

[17] Yoshida H, Sakka Y, Yamamoto T, Lebrun JM, Raj R. Densification behaviour and microstructural development in undoped yttria prepared by flash-sintering. *J Eur Ceram Soc*. 2014;**34**:991-1000. doi:10.1016/j.jeurceramsoc.2013.10.031.

[18] Caliman LB, Bichaud E, Soudant P, Gouvea D, Steil MC. A simple flash sintering setup under applied mechanical stress and controlled atmosphere. *MethodsX*. 2015;**2**:392-98. doi:10.1016/j.mex.2015.10.004.

[19] Mohebbi H, Mirkazemi SM. The effects of contact paste type and electric field on physical properties of zirconia bodies made by flash sintering method: Modeling via response surface methodology. *Iran J Mater Sci Eng*. 2020;**17**:93-102. doi:10.22068/IJMSE.17.4.93.

[20] Grimley CA, Prette ALG, Dickey EC. Effect of boundary conditions on reduction during early stage flash sintering of YSZ. *Acta Mater*. 2019;**174**:271-78. doi:10.1016/j.actamat.2019.05.001.

[21] Manière C, Lee G, Olevsky EA. Flash sintering of complex shapes. *Appl Mater Today*. 2022;**26**:101293. doi:10.1016/j.apmt.2021.101293.

[22] Storion AG, Lavagnini IR, Campos JV, Silva JGP, Maestrelli SC, Pallone EMJA. Effect of thermal insulation on microstructural homogeneity and onset temperature of flash sintered materials. *J Eur Ceram Soc*. 2021;**41**:7807-15. doi:10.1016/j.jeurceramsoc.2021.08.060.

[23] Lavagnini IR, Campos JV, Ferreira JA, Pallone EMJA. Microstructural evolution of 3YSZ flash□sintered with current ramp control. *J Am Ceram Soc*. 2020;**103**:3493-99. doi:10.1111/jace.17037.

[24] Jones GM, Biesuz M, Ji W, John SF, Grimley C, Manière C, Dancer CEJ. Promoting microstructural homogeneity during flash sintering of ceramics through thermal management. *MRS Bull*. 2021;**46**:59-66. doi:10.1557/s43577-020-00010-2.

[25] Campos JV, Lavagnini IR, Sousa RV, Ferreira JA, Pallone EMJA. Development of an instrumented and automated flash sintering setup for enhanced process monitoring and parameter control. *J Eur Ceram Soc*. 2019;**39**:531-38. doi:10.1016/j.jeurceramsoc.2018.09.002.

[26] Dancer CEJ. Flash sintering of ceramic materials. *Mater Res Express*. 2016;**3**:102001. doi:10.1088/2053-1591/3/10/102001.

[27] Biesuz M, Sglavo VM. Flash sintering of ceramics. *J Eur Ceram Soc*. 2019;**39**:115-43. doi:10.1016/j.jeurceramsoc.2018.08.048.

[28] Yu M, Grasso S, McKinnon R, Saunders T, Reece MJ. Review of flash sintering: materials, mechanisms and modelling. *Adv Appl Ceram*. 2017;**116**:24-60. doi:10.1080/17436753.2016.1251051.

[29] Ahmed RK, Saad EM, Fahmy HM, El Nashar RM. Multivariate experimental design: towards more reliable electrochemical detection. *Curr Opin Electrochem*. 2022;**31**:100880. doi:10.1016/j.coelec.2021.100880.

[30] Ait Baih M, Saffaj H, Aziz K, Bakka A, El Baraka N, Zidouh H, Mamouni R, Saffaj N. Statistical optimization of the elaboration of ceramic membrane support using Plackett-Burman and response surface methodology. *Mater Today Proc*. 2021. doi:10.1016/j.matpr.2021.11.269.

[31] Keramat E, Hashemi B. Modelling and optimizing the liquid phase sintering of alumina/CaO–SiO2–Al2O3 ceramics using response surface methodology. *Ceram Int*. 2021;**47**:3159-72. doi:10.1016/j.ceramint.2020.09.153.

[32] Sharif KM, Rahman MM, Azmir J, Mohamed A, Jahurul MHA, Sahena F, Zaidul ISM. Experimental design of supercritical fluid extraction – A review. *J Food Eng*. 2014;**124**:105-16. doi:10.1016/j.jfoodeng.2013.10.003.

[33] Mohebbi H, Mirkazemi SM. Influence of electric field strength on structure, microstructure, and electrical properties of flash sintered 8% mol Yttria-stabilized zirconia as a solid oxide fuel cell electrolyte. *Ceram Int*. 2021;**47**:20220-29. doi:10.1016/j.ceramint.2021.04.029.

[34] Xu W, Maksymenko A, Hasan S, Meléndez JJ, Olevsky E. Effect of external electric field on diffusivity and flash sintering of 8YSZ: A molecular dynamics study. *Acta Mater*. 2021;**206**:116596. doi:10.1016/j.actamat.2020.116596.

[35] Charalambous H, Jha SK, Vikrant KSN, García RE, Phuah XL, Wang H, Mukherjee A, Tsakalakos T. Electric field-induced grain boundary degradation mechanism in yttria stabilized zirconia. *Scr Mater*. 2021;**204**:114130.

doi:10.1016/j.scriptamat.2021.114130.

[36] Liu D, Li X, Liu F, Liu J, Gao Y, Ren K, Wang Y. Effect of the current density on the densification of 3 mol% yttria-stabilized zirconia in flash sintering. *J Alloys Compd*. 2020;**825**:154061. doi:10.1016/j.jallcom.2020.154061.

[37] ASTM C373. Standard Test Methods for Determination of Water Absorption and Associated Properties by Vacuum Method for Pressed Ceramic Tiles and Glass Tiles and Boil Method for Extruded Ceramic Tiles and Non-tile Fired Ceramic Whiteware Products. 2018. doi:10.1520/C0373-16.

[38] Du Y, Stevenson AJ, Vernat D, Diaz M, Marinha D. Estimating Joule heating and ionic conductivity during flash sintering of 8YSZ. *J Eur Ceram Soc*. 2016;**36**:749-59. doi:10.1016/j.jeurceramsoc.2015.10.037.

[39] Zhang J, Wang Z, Jiang T, Xie L, Sui C, Ren R, Qiao J, Sun K. Densification of 8 mol% yttria-stabilized zirconia at low temperature by flash sintering technique for solid oxide fuel cells. *Ceram Int*. 2017;**43**:14037-43. doi:10.1016/j.ceramint.2017.07.137.

[40] Campos JV, Lavagnini IR, Silva JGP, Ferreira JA, Sousa RV, Mücke R, Guillon O, Pallone EMJA. Flash sintering scaling-up challenges: Influence of the sample size on the microstructure and onset temperature of the flash event. *Scr Mater*. 2020;**186**:1-5. doi:10.1016/j.scriptamat.2020.04.022.

[41] Vendrell X, Yadav D, Raj R, West AR. Influence of flash sintering on the ionic conductivity of 8 mol% yttria stabilized zirconia. *J Eur Ceram Soc*. 2019;**39**:1352-58. doi:10.1016/j.jeurceramsoc.2018.12.048.

(Rec. 06-Jan-2025, Rev. 24-Jan-2025, 05-Feb-2025, Ac. 06-Feb-2025)

(AE: Daniel Z. de Florio)